2022-02-26

Single virus detection on silicon photonic crystal random cavities

Watanabe, K

10.1002/smll.202107597
Small
Wiley

Single virus detection on silicon photonic crystal random cavities

Keisuke Watanabe[1*], Hsin-Yu Wu[1], Jolly Xavier[1], Lovleen Tina Joshi[2], Frank Vollmer[1*]

1. Department of Physics and Astronomy, Living Systems Institute, University of Exeter, EX4 4QD, Exeter, UK
2. School of Biomedical Sciences, University of Plymouth, Plymouth PL4 8AA, UK

Abstract

On-chip silicon microcavity sensors are advantageous for the detection of virus and biomolecules due to their compactness and the enhanced light-matter interaction with the analyte. While their theoretical sensitivity is at the single-molecule level, the fabrication of high *Q* silicon cavities and their integration with optical couplers remain as major hurdles in applications such as single virus detection. Here, we propose and demonstrate the label-free single virus detection using silicon photonic crystal random cavities. The sensor chips consist of free-standing silicon photonic crystal waveguides and do not require pre-fabricated defect cavities or optical couplers. Residual fabrication disorder results in the Anderson-localized cavity modes which are excited by a free space beam. The $Q \sim 10^5$ is sufficient for observing the discrete step-changes in resonance wavelength for binding of single adenoviruses (~50 nm radius). The CMOS-compatible silicon sensor chips enable biosensors that operate at the level of single nanoparticles and molecules.

The worldwide viral pneumonia outbreak designated as coronavirus disease 2019 (COVID-19) has highlighted the importance of diagnostic and sensing methods for virions and viral molecules[1]. Sensors that can detect a virus rapidly can help track community spread and are emerging as vital tools in gaining control of global health emergencies such as the COVID-19 outbreak. Recent studies have shown the importance of optical sensors for the diagnoses of the severe acute respiratory syndrome-coronavirus-2 (SARS-CoV-2), the cause of COVID-19[1,2]. The photonic and plasmonic sensors have been used for the detection of coronavirus particles[3], their viral genomes[4], and the serological antibodies[5,6].

Optical microcavities such as the whispering-gallery-mode (WGM) optical resonators are highly versatile platforms for developing the optical biosensor applications. These micro-sensors can be fabricated in a compact format and integrated with microfluidics. In label-free WGM sensing, the analyte is typically detected from a wavelength shift or an intensity change that is caused by the attachment of a small number of biomolecules or nanoparticles to the cavity. WGMs excited in glass microspheres have already been used to demonstrate single influenza virus detection[19], followed by demonstrations of the detection of small nanoparticles[20], small virions[21], and single proteins[22 23].

The silicon-based photonic crystal (PhC) sensors[8–11] are a class of optical microcavities that can confine the light in particularly small mode volumes on the order of $(\lambda/n)^3$ and that enable the sensitive particle and molecule detection on chip[12]. Using the on-chip silicon PhC sensors, the detection of virus-sized single particles by the wavelength shift[11,13–16], antibody detection based on near-field optical trapping of virus particle[17] and the detection of virus by imaging-based techniques[18] have been demonstrated.

However, to best of our knowledge, the label-free detection of single virus from the optical shift of a silicon-based microcavity has not been previously reported. Although the PhC cavities have a figure of merit Q/V, where Q is the quality factor and V is the mode volume, that is larger than the Q/V of the WGM glass microspheres previously used for the single influenza virus sensing[19], there are challenges in fabricating the high Q/V cavity and assembling a functioning sensor chip for virus detection in an aqueous solution. Major hurdles have been the integration of an optical coupler for the excitation of the PhC cavity modes, the fabrication of microcavities of sufficiently high Q, the integration of plasmonic nanoparticles where the enhancement of sensitivity was required, and coupling the light in and out of the chip for real-time nanoparticle sensing[24]. Couplers such as optical fibers made use of edge-coupling using a spot size converter[25] or the tapered fiber coupling[26] in order to excite the microcavity/PhC structures. However, the addition of the fiber-based optical components complicated the measurement system and often limited the sensor's detection capability. Moreover, a fragile taper makes it often difficult to carry out the measurements in aqueous solution without breaking the fiber[27]. Furthermore, the binding of just a few particles to the taper can rapidly degrade the fiber transmission[28]. Detection of several nanoparticles without saturating a PhC microcavity response remains as another challenge.

To overcome these challenges and to achieve the real-time sensing of single virus with on-chip silicon microcavity sensors, we utilize silicon PhC *random* cavities in a conventional W1 waveguide[29,30] that are excited by a free space beam (Fig. 1a). Nanoparticle sensing with the Anderson-localized, random PhC cavities[30] provides several advantages as compared to the use of other, more carefully engineered PhC defect cavities[31] or the PhC heterostructure cavities[32,33]: (1) The silicon PhC sensor consists only of the W1 waveguide without requiring any other pre-fabricated optical structures such as defect cavities or coupler(s); (2) the residual and unavoidable fabrication disorder which usually limits a sensor's performance here localizes the light in the high Q/V random cavities; (3) the excitation of the random cavities along the guide using the free-space beam[34] requires only minimal initial beam alignment; (4) many particles can be detected without saturating the sensor response, and (5) the free-space excitation allows for ease of integration with an aqueous sample cell and, in the future, with microfluidics.

The random cavity modes along the W1 waveguide result from the Anderson localization of light[30,35–38] because of the coherent multi-scattering at the nanoscale fabrication imperfections of the PhC holes[39,40]. The length-scale of the fabrication disorder is on the order of a few nm in this work and as revealed by scanning electron microscopy (the root-mean-square deviation of air-hole roughness in this work was less < 6 nm). Due to the high Q factors on the order of 10^5 (ref. 41) and the small V on the order of $1(\lambda/n)^3$ (ref. 42), the Anderson-localized random cavities have previously been used for example in InGaAsP random lasers[43] and for quantum electrodynamics in GaAs PhC waveguides[35] to demonstrate the strong coupling with a single emitter[44,45]. Previously, we have demonstrated $Q > 10^5$ in silicon PhC W1 waveguide slabs in the telecom wavelength range at a similar level of nanoscale disorder[34,41], and predicted that the Anderson-localised random PhC microcavity sensor could provide a platform for various biosensing applications. Despite this potential for biosensing and nanoparticle detection in particular, there have been very few reports that use the Anderson-localized W1 random cavity modes for sensing applications. Previous works demonstrated the temperature sensing based on the thermo-optic effect of silicon[46] and the sensing of the bulk refractive index of the surrounding solution using PhC random cavities fabricated in Si_3N_4[47].

In this paper, we unveil the sensing characteristics of Anderson-localized modes in silicon PhC waveguide slabs which, at the Q of 10^5, are already sensitive enough to resolve virus-sized (radius ~50 nm) single particle binding events. We investigate the label-free detection capability with polystyrene particles and find the minimum detectable radius to be ~34 nm. We demonstrate the single virus particle detection with adenovirus, which has a radius of about 50 nm, with a signal to noise ratio of approximately 4. We find that an Anderson-localized random microcavity is capable of detecting many particle binding events despite its small modal volume on the order of $1(\lambda/n)^3$. We demonstrate the

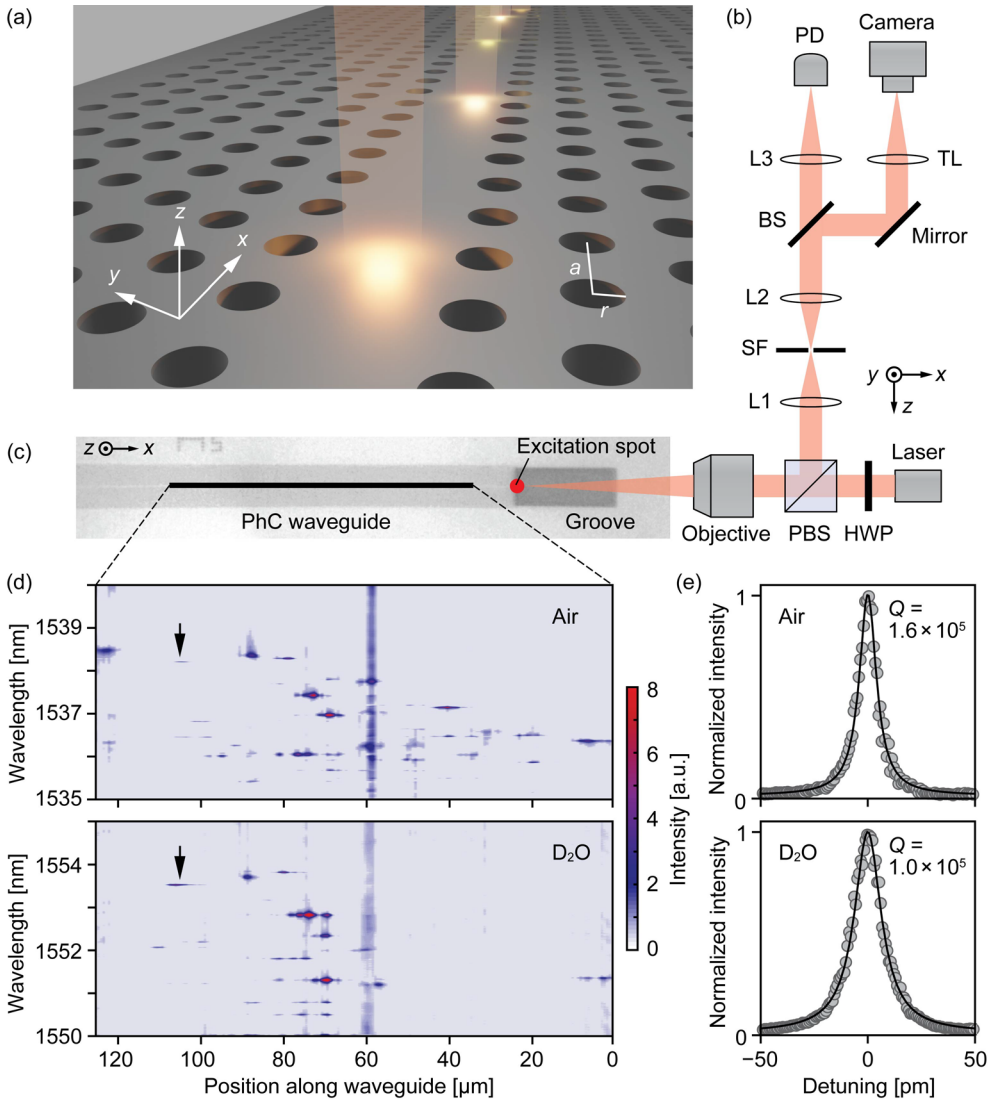

Fig. 1 Photonic crystal (PhC) random cavity. (a) Schematic illustration of the randomly distributed optical microcavities along the silicon W1 PhC waveguide; *a* and *r* indicate the lattice constant and air-hole radius, respectively. (b) Scheme of experimental setup for free-space excitation of Anderson-localized modes and (c) a microscopic image of a free-standing W1 PhC waveguide. A tightly focused laser beam with the polarization parallel to the waveguide (red arrow) is focussed from the vertical direction onto the end-facet of the waveguide (red dot) using a 40× objective (NA = 0.6). The vertically scattered light with a polarization that is perpendicular to the waveguide is analyzed using a InGaAs photodiode (PD) and an infrared camera. HWP, half wave plate; PBS, polarizing beam splitter; SP, spatial filter; L, lenses; TL, tube lens. (d) Spatially resolved spectra along the PhC waveguide in air (upper, excitation power P = 1 mW) and in D_2O (lower, P = 2 mW). The approximately 120 μm waveguide section that is imaged on the camera (line scan) is indicated by the black bold line in (c). (e) Representative spectra (gray dots) and the Lorentzian fit (black curves) used for the calculation of Q factors of the representative localized modes indicated with the black arrows in (d).

detection of up to 60 nanoparticle binding events from recording the step-wise changes in the resonance wavelength as the particles bind to the PhC sensor over the course of 20 min. This unexpected result shows that Anderson-localized cavities combine a very high detection sensitivity with a large detection bandwith, highly desirable sensing characteristics for developing on-chip biosensing applications.

Results

PhC random cavities. The PhC structure design used in our experiments is a standard W1 PhC waveguide obtained by leaving out air-holes along the Γ-K direction of the reciprocal-lattice[48]. Figure 1a shows the schematic of the device with the location of the random cavities highlighted. The PhC waveguide has a lattice constant of a = 410 nm and the normalized air-hole radius with r/a~0.3. For the excitation of localized modes, a tightly focused wavelength-tunable laser beam was focused from vertical direction onto the slab at the end-facet of a waveguide. As we have shown in the previous work, a polarization-tailored beam can excite Anderson localized modes[34] and the sensor response can be detected with sensitive InGaAs detectors despite the fact that the coupling efficiency is not as large when compared with the commonly-used side/butt coupling or the tapered-fiber coupling[49] methods. The spectrum of the high Q localized modes can be efficiently collected by tuning the laser wavelength and simultaneously recording the light scattered in the out-of-plane direction and focused on a photodetector (Fig. 1c). The infrared (IR) camera is used to image the location of the microcavities along the approx. 120 μm long

waveguide (Fig. 1d). The polarization direction of the linearly-polarized laser light was adjusted to the direction parallel to the waveguide to achieve a better coupling to the waveguide[34]. The residual fabrication disorder inherent in the silicon PhC induces both backscattering and out-of-plane scattering for the light propagating along the W1 waveguide, especially in the vicinity of the cut-off frequency where the radiation losses of the slowly guided Bloch-TE waveguide mode[46] increase[50,51]. As a result, one can vertically collect the scattered light using an objective to measure the spectrum of the localized modes for those *k*-vector components that lie within the numerical aperture (NA) of the objective. Since the localized cavities arise from the TE-like fundamental mode, the polarization direction of vertically scattered light is predominantly perpendicular to the waveguide. Thus, the localized modes can be collected by the photodetector using a polarizing beam splitter (PBS) while the background noise coming from the excitation laser is cut out by this cross-polarized configuration[52,53]. Different from other resonance scattering methods[54] in which the scattered light experiences Fano interference, our methods give rise to purely Lorentzian lineshapes because the excitation light and the scattered light do not propagate on the same optical path.

Figure 1d shows the spatial maps for the localized modes that were imaged by the IR camera as we step-wise change (sweep) the wavelength of the laser. The linescans were extracted from the images taken of the PhC while in air and after immersing the PhC slab in deuterium oxide (D_2O). The localized states appear in the images as the laser wavelength approaches the band edge of the TE-like W1 waveguide mode. The Anderson-localization of light is seen only in a narrow spectral window which is about 5 nm wide, in this example from about approx. 1550 nm to 1555 nm for a slab immersed in D_2O. We used D_2O instead of pure water (H_2O) to minimise absorption loss in water (see Supplementary Fig. S2 and Table. S1 for more details and for measurements in H_2O). Due to the increase in the refractive index in aqueous solution as compared to air, the localized modes are red-shifted in D_2O by about 15 nm. After immersing the sensor in the aqueous solution, we observed annihilation and generation of localized modes possibly because the altered refractive index changes the multiple scattering conditions in the waveguide. Figure 1e shows examples of the spectra obtained in air and in D_2O for the same PhC slab. Compared with the measurement in air (Q = 1.6 × 10^5), the Q factor slightly degrades in D_2O (Q = 1.0 × 10^5). We found that this Q is still high enough to carry out the nanoparticle sensing experiments.

Note that the air-holes of our PhC waveguides have approximately 4° sidewall tilt revealed by observation with a scanning electron microscope, which explains the quite efficient excitation of localized modes[41]. This vertical asymmetry of the sidewall causes polarization mixing when light propagates along the waveguide[55,56]. As a result, the ballistic TM-like mode can be converted to the TE-like fundamental mode at the intersection of the two modes where the group velocity of TE-like photonic band is small[41,57] and where the Anderson-localized modes appear. In this way, naturally created sidewall tilts and the modest unavoidable fabrication disorder in our sample favour the efficient excitation of the localized modes.

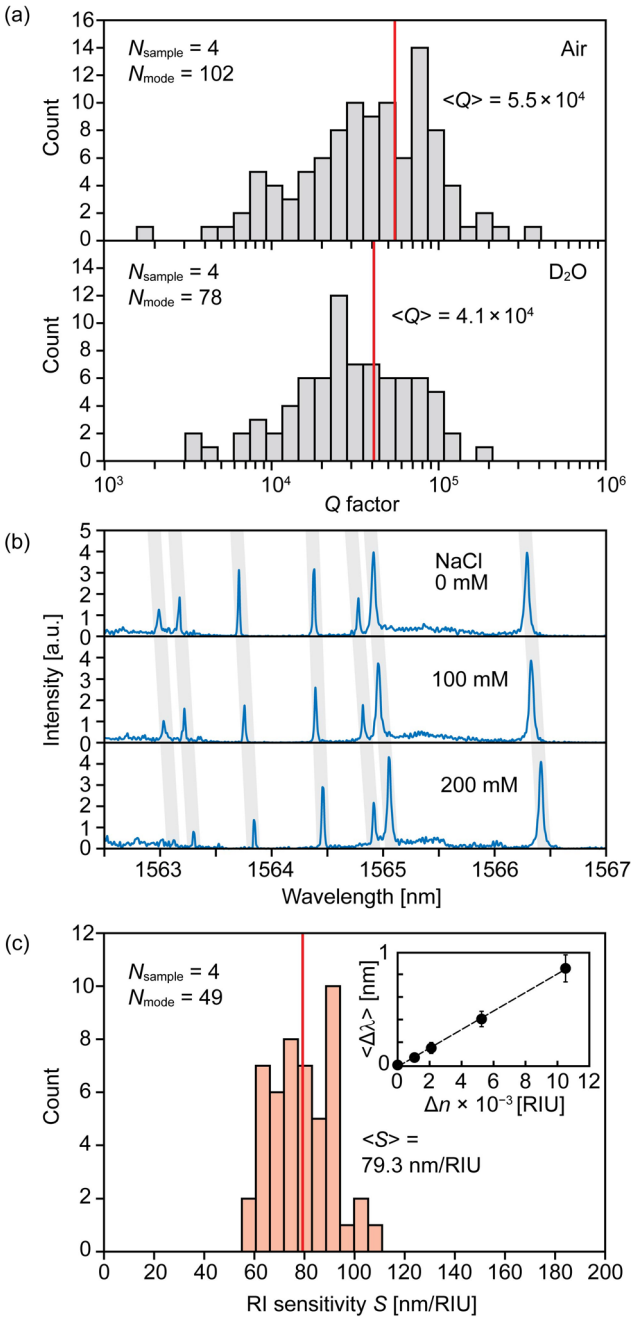

Fig. 2 Statistical analysis of *Q* factors and refractive index (RI) sensitivities. (a) Histograms of Q factors for the random microcavities measured in air and in D_2O. The Q factors were determined from a total of four different W1 PhC samples (N_{sample} = 4) with almost identical structural parameters a and r. The vertical red lines represent the average of Q factors (<Q>). (b) Examples of spectra measured in different NaCl concentrations. The thick grey lines serve as guide to the eye. (c) Histogram of RI sensitivities S. The vertical red line represents the average of S (<S>). Inset: The average wavelength shift (<$\Delta\lambda$>) as a function of RI change (Δn) of the solution.

We validate the Anderson-localization by analyzing the spatial distribution of the intensities of the light scattered by the random microcavities. Here, we consider the variance of the normalized intensity distribution var(I/<I>) where I is the intensity and <I> is the ensemble average of the intensity of the light scattered by one waveguide as identified by imaging. Anderson localization of PhC waveguides can also be

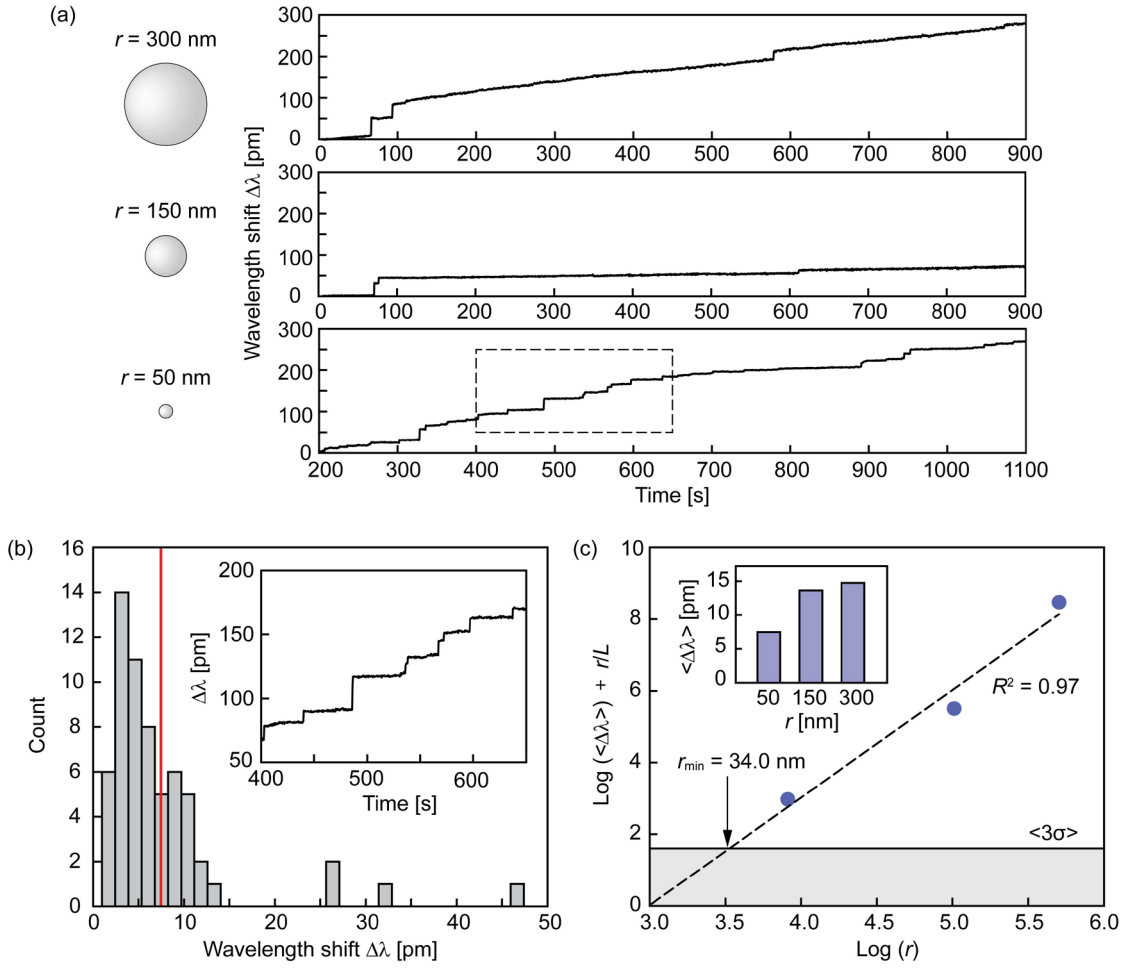

Fig. 3 Detection of single polystyrene (PS) particles. (a) Resonance wavelength shifts (Δλ) measured by injecting PS particles with radii 300 nm, 150 nm, and 50 nm. Each discrete step is associated with the adsorption of single PS particles onto the PhC waveguide. A single resonance peak of $Q = 4.0 \times 10^4$ in D_2O (100 mM NaCl) was tracked in real-time in these experiments. (b) Histogram of wavelength shifts for r = 50 nm. The vertical red line represents the average of Δλ. The inset shows the zoomed in view of the enclosed region in (a). (c) The measured <Δλ> and the linear fit for different r. The average noise of the wavelength traces <3σ> is indicated by the black horizontal line. Minimum detectable PS particle radius r_{min} = 34.0 nm was obtained at the intersection of the two lines. Inset: The average of the Δλ ????? (<Δλ>) as a function of r.

characterized by the localization length, which is determined from the exponential decay of the electromagnetic field of the near field[38], however, the measurement is not always a simple task. For example, it is difficult to discern if the decay originates from the effects of the coherent scattering processes or the material absorption. The alternative Anderson localization criterion has been introduced which makes it possible to analyse the variance of the intensities in a spectrum and show that var(I/<I>) > 7/3 for Anderson-localization which holds even under the presence of the material absorption[58]. We confirm that this condition is met for our PhC waveguides in a 10 nm spectral window containing the localised modes. We find var(I/<I>) = 14.4 in air and var(I/<I>) = 3.41 in D_2O (see details in Supplementary Fig. S1).

Statistical characterization of the random microcavities. Q factors of localized modes in air and D_2O were extracted from four different PhC waveguides (N_{sample} = 4) by the Lorentzian fits. Figure 2a shows the histograms. The average of the Q factors in D_2O (<Q> = 4.1×10^4) decreased compared to the measurements in air (<Q> = 5.5×10^4) due to the reduced refractive index difference between the silicon PhC slab and external medium. At the same time, the total number of localized modes (N_{mode}) in D_2O was smaller than those observed in air, which was consistent with a spatial map of the light scattered from the optical microcavities imaged in Fig. 1d. Notably, the maximum Q factor was 3.4×10^5 in air and 2.0×10^5 in D_2O. These values are in fact close to the ideal $Q \sim 10^6$ imposed by scattering loss[59] in PhC cavities, indicating that Q factors of Anderson localized modes in silicon PhC waveguides are comparable to those that would be obtained in carefully engineered and fabricated defect cavities. Next, we measured the wavelength shifts of the localized modes by changing the NaCl concentrations in D_2O, as shown in Fig. 2b. As expected, the peak positions of localized modes red-shifted in wavelength with increasing solution refractive index. Although some peaks seem to have split or disappeared, bulk refractive index sensitivities S [nm/RIU] were evaluated, where possible, from the slope of the wavelength shifts Δλ versus the refractive index changes Δn. From the histogram in Fig. 2c, the average of S (<S>) was determined to be 79.3 nm/RIU.

S can be estimated from $S = \Gamma_{env}(\lambda_0/n_{eff})$ where Γ_{env} is the confinement factor of the electric field energy stored in the surrounding medium, λ_0 is the cavity resonance wavelength, and n_{eff} is the effective refractive index of the cavity mode[60,61]. Our random cavities have a few times smaller S compared with well-engineered PhC defect cavities which are as high as $S > 500$ nm/RIU[9,62], which in turn indicates that the Anderson-localized modes are tightly confined inside the silicon slab, i.e., a large Q and small Γ_{env}. The slight deviation in S among different random cavities can be accounted for from the fact that each cavity has different Γ_{env} and n_{eff}. Considering a commonly used figure of merit (FOM) expressed as S/FWHM [/RIU] where FWHM is the full width at half maximum[63], our random cavities reach up to FOM = 1.0 x 10^4/RIU in D_2O. The refractive index sensing with Anderson localized modes was first reported in 2017 using Si_3N_4 PhC waveguide[47], but the FOM~270 /RIU was not as large as it is the case here. This can be attributed to the smaller Q factors of Si_3N_4-based cavity modes which is expected because of the refractive index of Si_3N_4 ($n \sim 2$) which is much smaller than that of Si ($n \sim 3.5$).

At the same Q factor of a microcavity, a smaller mode volume V would give a larger wavelength shift[64]. Although it is difficult to extract individual V of Anderson-localized modes experimentally, theoretical works have shown that the smallest V reaches around $1(\lambda/n)^3$, which corresponds to the diffraction-limited mode volume[42]. Therefore, Q/V is expected to reach up to 2.0 x 10^5 $(n/\lambda)^{-3}$ in D_2O in our case. As it will be shown next, this Q/V is sufficiently large to detect single particles and virus. Also, this value is competitive with an engineered one-dimensional PhC (Q/V = 3.0 x 10^5 $(n/\lambda)^{-3}$) nanobeam cavity[15] where it was demanded to employ side coupling using an optical fiber. It should be noted here that further enhancement of Q/V has been experimentally demonstrated with hybrid plasmonic-photonic systems[12,65], enabling monitoring of single protein interactions[12].

Detection of single polystyrene particles. To demonstrate detection of single polystyrene (PS) particles, PS nanoparticles with the different radii of r = 300 nm, 150 nm, and 50 nm were injected into the sample cell. The silicon PhC surface was not functionalized, the nanoparticle adsorption to the silicon relies entirely on electrostatic interactions of the silicon surface and the PS particles (see Materials and Methods). Figure 3a shows the wavelength shifts that we tracked for a representative Anderson-localized cavity with a 200 ms time resolution. Discrete wavelength steps were observed for all particle sizes and the step heights increased with increasing particle radius r. As we will validate later, these steps are associated with single PS binding events. Although the injected PS concentration c was exactly the same for all r (c = 100 µg/mL) there was a significant difference in the average rate at which the steps were observed Keisuke: worth mentioning the particle concentration in units of pM which is different? (Supplementary Fig. S3). Specifically, for r = 300 nm and 150 nm PS particles, the step rates of 0.0044 s^{-1} were small, and the binding events saturated quickly, after approximately 5 particles were adsorbed because the particle sizes were large in comparison with the cavity and waveguide size. On the other hand, for r = 50 nm PS particles, step rates were 0.054 s^{-1} and a large number of approximately 60 particles were

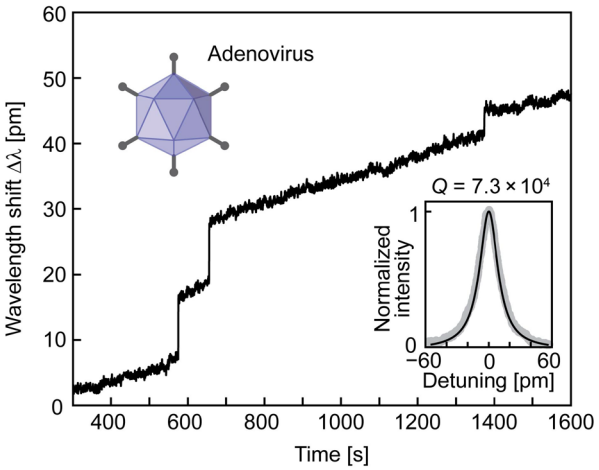

Fig. 4 Detection of single adenoviruses. The resonance wavelength shift (pm) vs. time (s). Inset: The measured resonance peak (gray dots) with $Q = 7.3 \times 10^4$ in D_2O (100 mM NaCl) and the corresponding Lorentzian fit (black curve).

able to be detected from the shift of the cavity in the 20 min measurement time (Supplementary Fig. S4). This result suggests that PS particles that adsorb outside of the near-field/mode volume of the sensing cavity also affect the wavelength shift. A detailed investigation of the physical mechanism is needed and lies outside the scope of this manuscript. Note that the gradual and slight drifts of the resonance wavelengths towards a longer wavelength could be attributed to many factors including oxidation of the silicon surface, temperature increase, slight movement of the optical setup, and the evaporation of the sample solution over time[14]. Figure 3b shows the histogram (number of steps N = 62) obtained in a ~20 min measurement window for r = 50 nm PS particles. Most of the steps were smaller than 15 nm, and the average step height $\langle\Delta\lambda\rangle$ was approximately 7.5 nm. The average step height for the different size PS particles is shown in the inset of Fig. 3c. There was no large difference for the average steps hights that were observed for r = 150 nm and 300 nm PS particles. This can be attributed to the fact that the PS particles size is large compared with the evanescent decay length L of the cavity modes (L = 52 nm). For particle radii of tens to hundreds of nm, the wavelength shift of a microcavity $\Delta\lambda$ is estimated from r and L as follows[14,19]: $\Delta\lambda \propto r^3 e^{-r/L}$. By transforming this, one can obtain $\log(\langle\Delta\lambda\rangle) + r/L = 3\log(r) + constant.$, which has a linear slope of approximately 3 in the log-log plot. Figure 3c shows a linear fit of the experimental results. When L = 52 nm, the correlation coefficient R^2 was 0.97, showing a good agreement between the experiment and theory. This result clearly confirmed that discrete steps were caused by adsorption of single particles. Furthermore, we evaluated the minimum detectable PS particle radius r_{min} to be 34.0 nm from the intersection of the linear fit and the average noise of the wavelength trace $\langle 3\sigma \rangle$, where σ is the standard deviation, calculated by 10 points in the trace.

Detection of single viruses. The adenovirus solution was injected into a sample chamber and we tracked the wavelength shift of a representative localized mode with Q =

7.3×10^4 in D_2O. As shown in Fig. 4, three different discrete steps were observed in a ~30 min measurement. Note that, similar to the detection of PS particles, the interaction between the silicon surface and the virions relies on the electrostatic interactions between them. To check the reproducibility, we repeated the same measurements three times and obtained the average step height $<\Delta\lambda>$ of 3.9 nm. Since adenoviruses have a radius of 35-50 nm[66] and a refractive index smaller than that of PS (~1.59)[67], this step height conforms to the theoretical estimate.

The average noise in the wavelength traces $<3\sigma>$ was determined to be 1.0 pm, and thus the signal-to-noise ratio (SNR) for single adenovirus sensing was ~4. Although this value was sufficient to resolve single viruses, the SNR could be improved further by increasing either the *Q* factor or the peak intensity of the localized mode at the surface of the PhC[61]. In our present study, $<3\sigma>$ was about 1/20th the FWHM, but it is predicted to be reduced down to 1/2000th the FWHM in an ideal setting for a PhC cavity[68], which would be 100 times better as it is the case here. Improving the sensor response would help more with the reliable detection of single viruses and discriminating their sizes.

Discussion In this study, we have demonstrated label-free single virus detection on silicon PhC random cavities. The Anderson-localized cavities are excited in W1 PhC waveguides and have resonance *Q* factors of $\sim 10^5$ in D_2O. The single particle detection capability has been confirmed by detecting different sizes of PS particles and single adenoviruses. Given the present experimental parameters, the minimum detectable PS particle radius has been estimated to be around 34 nm. Our high *Q*/*V* PhC cavities are excited by a free-space beam and without the need of elaborate structural optimizations and integration of gratings or delicate fiber couplers, needed in sensing applications with well-engineered PhC defect cavities. One of the limitations of the proposed sensing method is that it is currently not possible to predict the exact number and locations of each of the detectable localized modes. Thus, we have to use imaging to find the random cavities and their location along the guide. Furthermore, because of the large free-spectral range it is difficult to currently track multiple random cavity modes simultaneously. This issue can be addressed by using a larger-bandwidth piezo tuning laser source. The random microcavities can be excited by focussing a fixed single beam onto the W1 waveguide end-facet, which enables multiplexed detection without the need for the spatial scanning of the laser beam.

Taking into account the fact that the presented silicon PhC waveguides are CMOS compatible and made of comparatively inexpensive silicon-on-insulator wafers, this platform may become important for the future on-chip diagnostic devices that require the single particle detection capabilities. We envisage that the detection of specific interactions between intact virions and the sensor surface functionalized with a specific antibody or an aptamer[69] will enable a high specificity for the multiplexed virus sensing applications. Finally, we should emphasize that isolated PhC chips can be readily integrate with microfluidics that allow the detection with small sample volumes and utilising multiple sample channels via automated sample input/output systems[70]. Thus, on-chip virus diagnostic devices with multiplexed detection systems are potentially realizable. The sensitivity range could be extended to the single-molecule level in optoplasmonic Anderson localised PhC microcavities[24]. While our current work is devoted to the detection of single viruses on a simple sensor chip, sensing of single protein sets one of the future directions for this work.

Materials and methods

Device Fabrication and characterization. W1 PhC waveguides were fabricated on silicon-on-insulator wafers with a silicon layer of 220 nm thickness. The details of the fabrication process are described elsewhere[46]. Briefly, the triangular lattice PhC patterns, where a line of air-holes was left out to realize W1 waveguide, were defined by electron-beam lithography and then transferred into the wafers using chlorine-based inductively coupled plasma reactive ion etching. The buried oxide layer was finally removed with buffered hydrofluoric acid to form a free-standing PhC slab. Random cavities in the PhC waveguide were excited using a 40× objective (Nikon, NA = 0.6) where the wavelength-scanning of the impinged beam from a tunable laser was realized by means of built-in motor (Ando, AQ4320D) for broadband excitation (1480–1580 nm, 100 kHz linewidth and 1 pm tuning resolution). The out-of-plane scattering of the cavity modes was imaged and recorded by an InGaAs camera (Sensors Unlimited, 320CSX). Once a sharp resonance peak to be used for a single particle sensing experiment was determined, the excitation source was switched to a tunable laser (Spectra Quest Lab, λ-lock) equipped with piezo to precisely scan the wavelengths (1460–1600 nm). A function generator (Hewlett-Packard) was connected to the laser controller to perform the piezo scan with a triangular waveform at 5 Hz for a frequency range of ~100 GHz. The reference signal and the resonance spectra measured with a 1.0 mm diameter InGaAs PD (Edmund Optics, #59-198) at room temperature were acquired by a data acquisition system (National Instruments), and the peak positions were recorded by Lorentzian fitting in real-time.

Detection of single particles. The sample cell was made by tightly sandwiching a silicone rubber sheet between a glass slide and a cover slip after their air plasma treatment. Then, a PhC sample was fixed into the cell by using a silicone glue for measurement in aqueous solution. PS particles solution (Alpha Nanotech, 10 mg/mL, carboxylated) were first centrifuged at 10,000 rpm for 10-15 min and the pellet was resuspended in D_2O (Merck, 151882). It was then dispersed in an ultrasonic bath for 5 min to separate individual particles. The solution was injected into the sample cell (300 µL) to a final concentration of 100 µg/mL. To minimize the repulsive force between the PS particles and the silicon PhC surface, the solution pH was adjusted to pH~2 in 100 mM NaCl. Only when comparing the results with different sizes of PS particles (Fig. 3), the PS particles were removed from the device by heating it in acetone at 70°C for 20 min, in order to repeat the experiment using the same localized mode. Adenovirus sample was provided by University of Plymouth, and the sample solution was injected into the sample cell (pH~7, 100 mM NaCl) at a dilution of 1/25.

Preparation of adenovirus solution. Adenovirus vector strain Ad5-GFP, a replication defective Ad5 that does not express Adenovirus early region 1A (E1A), was also used as analyte for single particle sensing. Adenovirus is a common virus that typically cause colds or flu-like symptoms in those infected. Ad5-GFP was obtained via collaboration and grown and purified as described previously[71]. Typical sizes of adenovirus are 100 nm in diameter. The samples were inactivated via germicidal UV-C light at a wavelength of 253.7 nm. The concentration of viral particles was of 1 x 10^9 pfu/ml.

Data availability. All data files and PhC design files are available upon reasonable request to the corresponding author.

References

1. Kevadiya, B. D. *et al.* Diagnostics for SARS-CoV-2 infections. *Nat. Mater. 2021 205* **20**, 593–605 (2021).

2. Toropov, N. *et al.* SARS-CoV-2 Tests: Bridging the Gap between Laboratory Sensors and Clinical Applications. *ACS Sensors* acssensors.1c00612 (2021) doi:10.1021/ACSSENSORS.1C00612.

3. Huang, L. *et al.* One-step rapid quantification of SARS-CoV-2 virus particles via low-cost nanoplasmonic sensors in generic microplate reader and point-of-care device. *Biosens. Bioelectron.* **171**, 112685 (2021).

4. Qiu, G. *et al.* Dual-Functional Plasmonic Photothermal Biosensors for Highly Accurate Severe Acute Respiratory Syndrome Coronavirus 2 Detection. *ACS Nano* **14**, 5268–5277 (2020).

5. Zhao, B., Che, C., Wang, W., Li, N. & Cunningham, B. T. Single-step, wash-free digital immunoassay for rapid quantitative analysis of serological antibody against SARS-CoV-2 by photonic resonator absorption microscopy. *Talanta* **225**, 122004 (2021).

6. Lew, T. T. S. *et al.* Epitope-Functionalized Gold Nanoparticles for Rapid and Selective Detection of SARS-CoV-2 IgG Antibodies. *ACS Nano* (2021) doi:10.1021/acsnano.1c04091.

7. Subramanian, S., Wu, H.-Y., Constant, T., Xavier, J. & Vollmer, F. Label-Free Optical Single-Molecule Micro- and Nanosensors. *Adv. Mater.* **30**, 1801246 (2018).

8. Lee, M. R. & Fauchet, P. M. Two-dimensional silicon photonic crystal based biosensing platform for protein detection. *Opt. Express* **15**, 4530 (2007).

9. Scullion, M. G., Krauss, T. F. & Di Falco, A. Slotted photonic crystal sensors. *Sensors (Switzerland)* vol. 13 3675–3710 (2013).

10. Pal, S. *et al.* Selective virus detection in complex sample matrices with photonic crystal optical cavities. *Biosens. Bioelectron.* **44**, 229–234 (2013).

11. Baker, J. E., Sriram, R. & Miller, B. L. Recognition-mediated particle detection under microfluidic flow with waveguide-coupled 2D photonic crystals: Towards integrated photonic virus detectors. *Lab Chip* **17**, 1570–1577 (2017).

12. Liang, F., Guo, Y., Hou, S. & Quan, Q. Photonic-plasmonic hybrid single-molecule nanosensor measures the effect of fluorescent labels on DNA-protein dynamics. *Sci. Adv.* **3**, (2017).

13. Lin, S. & Crozier, K. B. Trapping-assisted sensing of particles and proteins using on-chip optical microcavities. *ACS Nano* **7**, 1725–1730 (2013).

14. Quan, Q. *et al.* Single particle detection in CMOS compatible photonic crystal nanobeam cavities. *Opt. Express* **21**, 32225 (2013).

15. Wang, C., Quan, Q., Kita, S., Li, Y. & Lončar, M. Single-nanoparticle detection with slot-mode photonic crystal cavities. *Appl. Phys. Lett.* **106**, (2015).

16. Liang, F. & Quan, Q. Detecting Single Gold Nanoparticles (1.8 nm) with Ultrahigh- *Q* Air-Mode Photonic Crystal Nanobeam Cavities. *ACS Photonics* **2**, 1692–1697 (2015).

17. Kang, P., Schein, P., Serey, X., O'Dell, D. & Erickson, D. Nanophotonic detection of freely interacting molecules on a single influenza virus. *Sci. Rep.* **5**, 12087 (2015).

18. Li, N. *et al.* Photonic resonator interferometric scattering microscopy. *Nat. Commun.* **12**, 1–9 (2021).

19. Vollmer, F., Arnold, S. & Keng, D. Single virus detection from the reactive shift of a whispering-gallery mode. *Proc. Natl. Acad. Sci. U. S. A.* **105**, 20701–20704 (2008).

20. Shopova, S. I., Rajmangal, R., Holler, S. & Arnold, S. Plasmonic enhancement of a whispering-gallery-mode biosensor for single nanoparticle detection. *Appl. Phys. Lett.* **98**, (2011).

21. Dantham, V. R., Holler, S., Kolchenko, V., Wan, Z. & Arnold, S. Taking whispering gallery-mode single virus detection and sizing to the limit. *Appl. Phys. Lett.* **101**, 043704 (2012).

22. Dantham, V. R. *et al.* Label-free detection of single protein using a nanoplasmonic-photonic hybrid microcavity. *Nano Lett.* **13**, 3347–3351 (2013).

23. Vollmer, F. & Yu, D. *Optical Whispering Gallery Modes for Biosensing*. (Springer International Publishing, 2020). doi:10.1007/978-3-030-60235-2.

24. Xavier, J., Vincent, S., Meder, F. & Vollmer, F. Advances in optoplasmonic sensors - Combining optical nano/microcavities and photonic crystals with plasmonic nanostructures and nanoparticles. *Nanophotonics* **7**, 1–38 (2018).

25. Moll, N., McNab, S. J. & Vlasov, Y. A. Ultra-low loss

photonic integrated circuit with membrane-type photonic crystal waveguides. *Opt. Express, Vol. 11, Issue 22, pp. 2927-2939* **11**, 2927–2939 (2003).

26. Scullion, M. G., Fischer, M. & Krauss, T. F. Fibre Coupled Photonic Crystal Cavity Arrays on Transparent Substrates for Spatially Resolved Sensing. *Photonics 2014, Vol. 1, Pages 412-420* **1**, 412–420 (2014).

27. Kim, E., Baaske, M. D. & Vollmer, F. Towards next-generation label-free biosensors: recent advances in whispering gallery mode sensors. *Lab Chip* **17**, 1190–1205 (2017).

28. Zhu, J., Özdemir, Ş. K. & Yang, L. Optical detection of single nanoparticles with a subwavelength fiber-taper. *IEEE Photonics Technol. Lett.* **23**, 1346–1348 (2011).

29. Baba, T. *et al.* Light propagation characteristics of straight single-line-defect waveguides in photonic crystal slabs fabricated into a silicon-on-insulator substrate. *IEEE J. Quantum Electron.* **38**, 743–752 (2002).

30. Topolancik, J., Ilic, B. & Vollmer, F. Experimental Observation of Strong Photon Localization in Disordered Photonic Crystal Waveguides. *Phys. Rev. Lett.* **99**, 253901 (2007).

31. Zhang, Y. N., Zhao, Y. & Lv, R. Q. A review for optical sensors based on photonic crystal cavities. *Sensors and Actuators, A: Physical* vol. 233 374–389 (2015).

32. Song, B.-S., Noda, S., Asano, T. & Akahane, Y. Ultra-high-Q photonic double-heterostructure nanocavity. *Nat. Mater. 2005 43* **4**, 207–210 (2005).

33. Di Falco, A., O'Faolain, L. & Krauss, T. F. Chemical sensing in slotted photonic crystal heterostructure cavities. *Appl. Phys. Lett.* **94**, 063503 (2009).

34. Mahdavi, A. *et al.* Free space excitation of coupled Anderson-localized modes in photonic crystal waveguides with polarization tailored beam. *Appl. Phys. Lett.* **110**, (2017).

35. Sapienza, L. *et al.* Cavity Quantum Electrodynamics with Anderson-Localized Modes. *Science (80-.).* **327**, 1352–1355 (2010).

36. Thyrrestrup, H., Smolka, S., Sapienza, L. & Lodahl, P. Statistical Theory of a Quantum Emitter Strongly Coupled to Anderson-Localized Modes. *Phys. Rev. Lett.* **108**, 113901 (2012).

37. Liu, J. *et al.* Random nanolasing in the Anderson localized regime. *Nat. Nanotechnol.* **9**, 285–289 (2014).

38. García, P. D., Kiršanskė, G., Javadi, A., Stobbe, S. & Lodahl, P. Two mechanisms of disorder-induced localization in photonic-crystal waveguides. *Phys. Rev. B* **96**, 144201 (2017).

39. Le Thomas, N. *et al.* Light transport regimes in slow light photonic crystal waveguides. *Phys. Rev. B* **80**, 125332 (2009).

40. Mazoyer, S., Hugonin, J. P. & Lalanne, P. Disorder-Induced Multiple Scattering in Photonic-Crystal Waveguides. *Phys. Rev. Lett.* **103**, 063903 (2009).

41. Topolancik, J., Vollmer, F., Ilic, R. & Crescimanno, M. Out-of-plane scattering from vertically asymmetric photonic crystal slab waveguides with in-plane disorder. *Opt. Express* **17**, 12470 (2009).

42. Vasco, J. P. & Hughes, S. Statistics of Anderson-localized modes in disordered photonic crystal slab waveguides. *Phys. Rev. B* **95**, 224202 (2017).

43. Liu, J. *et al.* Random nanolasing in the Anderson localized regime. *Nat. Nanotechnol.* **9**, 285–289 (2014).

44. Thyrrestrup, H., Smolka, S., Sapienza, L. & Lodahl, P. Statistical theory of a quantum emitter strongly coupled to Anderson-localized modes. *Phys. Rev. Lett.* **108**, (2012).

45. Gao, J. *et al.* Strongly coupled slow-light polaritons in one-dimensional disordered localized states. *Sci. Rep.* **3**, 1–6 (2013).

46. Vollmer, F. & Topolancik, J. Disorder-induced high-Q cavities in photonic crystal waveguides. in *Laser Resonators and Beam Control X* (eds. Kudryashov, A. V., Paxton, A. H. & Ilchenko, V. S.) vol. 6872 68720X (International Society for Optics and Photonics, 2008).

47. Trojak, O. J., Crane, T. & Sapienza, L. Optical sensing with Anderson-localised light. *Appl. Phys. Lett.* **111**, 141103 (2017).

48. Notomi, M. *et al.* Extremely large group-velocity dispersion of line-defect waveguides in photonic crystal slabs. *Phys. Rev. Lett.* **87**, 253902-253902–4 (2001).

49. Dutta, H. S., Goyal, A. K., Srivastava, V. & Pal, S. Coupling light in photonic crystal waveguides: A review. *Photonics and Nanostructures - Fundamentals and Applications* vol. 20 41–58 (2016).

50. Kuramochi, E. *et al.* Disorder-induced scattering loss of line-defect waveguides in photonic crystal slabs. *Phys. Rev. B - Condens. Matter Mater. Phys.* **72**, 161318 (2005).

51. O'Faolain, L. *et al.* Dependence of extrinsic loss on group velocity in photonic crystal waveguides. *Opt. Express* **15**, 13129 (2007).

52. Rivoire, K., Faraon, A. & Vuckovic, J. Gallium phosphide photonic crystal nanocavities in the visible. *Appl. Phys. Lett.* **93**, 063103 (2008).

53. Englund, D. *et al.* Resonant excitation of a quantum dot strongly coupled to a photonic crystal nanocavity. *Phys. Rev. Lett.* **104**, 073904 (2010).

54. Galli, M. *et al.* Light scattering and Fano resonances

in high-Q photonic crystal nanocavities. *Appl. Phys. Lett.* **94**, 071101 (2009).

55. Tanaka, Y., Asano, T., Akahane, Y., Song, B. S. & Noda, S. Theoretical investigation of a two-dimensional photonic crystal slab with truncated cone air holes. *Appl. Phys. Lett.* **82**, 1661–1663 (2003).

56. Canning, J. *et al.* Mapping the broadband polarization properties of linear 2D SOI photonic crystal waveguides. *Opt. Express* **15**, 15603 (2007).

57. Huisman, S. R. *et al.* Measurement of a band-edge tail in the density of states of a photonic-crystal waveguide. *Phys. Rev. B* **86**, 155154 (2012).

58. Chabanov, A. A., Stoytchev, M. & Genack, A. Z. Statistical signatures of photon localization. *Nature* **404**, 850–853 (2000).

59. Simbula, A. *et al.* Realization of high- *Q* / *V* photonic crystal cavities defined by an effective Aubry-André-Harper bichromatic potential. *APL Photonics* **2**, 056102 (2017).

60. Zhu, H., White, I. M., Suter, J. D., Dale, P. S. & Fan, X. Analysis of biomolecule detection with optofluidic ring resonator sensors. *Opt. Express* **15**, 9139 (2007).

61. White, I. M. & Fan, X. On the performance quantification of resonant refractive index sensors. *Opt. Express* **16**, 1020 (2008).

62. Pitruzzello, G. & Krauss, T. F. Photonic crystal resonances for sensing and imaging. *J. Opt. (United Kingdom)* **20**, (2018).

63. Anker, J. N. *et al.* Biosensing with plasmonic nanosensors. *Nat. Mater.* **7**, 442–453 (2008).

64. Arnold, S., Khoshsima, M., Teraoka, I., Holler, S. & Vollmer, F. Shift of whispering-gallery modes in microspheres by protein adsorption. *Opt. Lett.* **28**, 272 (2003).

65. Conteduca, D. *et al.* Ultra-high Q/V hybrid cavity for strong light-matter interaction. *APL Photonics* **2**, 086101 (2017).

66. Saha, B., Wong, C. M. & Parks, R. J. The Adenovirus Genome Contributes to the Structural Stability of the Virion. *Viruses 2014, Vol. 6, Pages 3563-3583* **6**, 3563–3583 (2014).

67. Pang, Y., Song, H. & Cheng, W. Using optical trap to measure the refractive index of a single animal virus in culture fluid with high precision. *Biomed. Opt. Express* **7**, 1672 (2016).

68. Saurav, K. & Le Thomas, N. Probing the fundamental detection limit of photonic crystal cavities. *Optica* **4**, 757 (2017).

69. Nguyen, V. T. *et al.* Highly sensitive sandwich-type SPR based detection of whole H5Nx viruses using a pair of aptamers. *Biosens. Bioelectron.* **86**, 293–300 (2016).

70. Liao, Z. *et al.* Microfluidic chip coupled with optical biosensors for simultaneous detection of multiple analytes: A review. *Biosens. Bioelectron.* **126**, 697–706 (2019).

71. Fejér, G. *et al.* Adenovirus Infection Dramatically Augments Lipopolysaccharide-Induced TNF Production and Sensitizes to Lethal Shock. *J. Immunol.* **175**, 1498–1506 (2005).

Acknowledgements

F.V. acknowledges the funding from EPSRC EP/R031428/1. K.W. kindly acknowledges Monika Pietrzyk, Nikita Toropov, and Eleanor Osborne for valuable discussion with the design of experiments. The authors thank Gillian Fearnyough for proofreading the manuscript.

Author contributions

F.V. conceived the experiment and supervised the project; K.W, H-Y.W., J.X., and F.V. designed the experiments, T.J. provided adenovirus sample and assisted the experiments, K.W. conducted the experiments and analyzed the results, K.W. and F.V. co-wrote the manuscript with contributions from all the authors.

Competing financial interests

The authors declare no competing financial interests.